Triple-enhanced Raman Scattering Sensors from Flexible MXene/Au Nanocubes Platform via Attenuating the Coffee Ring Effect

Xin Liu[1,2], *Alei Dang*[1,2]*, *Tiehu Li*[1,2]*, *Tung-Chun Lee*[3,4], *Yiting Sun*[1,2], *Yuhui Liu*[1,2], *Fei Ye*[1,2], *Shuze Ma*[1], *Yong Yang*[1], *Weibin Deng*[1,2]

[1.] School of Materials Science and Engineering, Northwestern Polytechnical University, Xi'an 710072, P. R China.

[2.] Shannxi Engineering laboratory for Graphene New Carbon Materials and Applications, School of Materials Science and Engineering, Northwestern Polytechnical University, Xi'an 710072, P. R China.

[3.] Department of Chemistry, University College London (UCL), London WC1H 0AJ, U.K.

[4.] Institute for Materials Discovery, University College London, London, WC1H 0AJ, UK.

*Corresponding author: Alei Dang, Tiehu Li

E-mail address: dangalei@nwpu.edu.cn; litiehu@nwpu.edu.cn;

Abstract: Developing substrates that combine sensitivity and signal stability is a major challenge in surface enhanced Raman scattering (SERS) research. Herein, we present a flexible triple-enhanced Raman Scattering MXene/Au nanocubes (AuNCs) sensor fabricated by selective filtration of $Ti_3C_2T_x$ MXene/AuNCs hybrid on the $Ti_3C_2T_x$ MXene membrane and subsequent treatment with 1H,1H,2H,2H-perfluoro-octyltriethoxysilane (FOTS). The resultant superhydrophobic MXene/AuNCs-FOTS membrane not only provides the SERS substrate with environmental stability, but also imparts analyte enrichment to enhance the sensitivity (LOD = 1×10^{-14} M) and reliability (RSD = 6.41 %) for Rhodamine 6G (R6G) molecules owing to the attenuation of the coffee ring effect. Moreover, the triple enhancement mechanism of combining plasmonic coupling enhancement from plasmonic coupling (EM) of nearby AuNCs at lateral and longitudinal direction of MXene/AuNCs-FOTS membrane, charge transfer (CT) from $Ti_3C_2T_x$ MXene and target molecules and analyte enrichment function provides the substrate with excellent SERS performance (EF=3.19×10^9), and allows efficient quantification of biomarkers in urine. This work could provide new insights into MXenes as building blocks for high-performance substrates and fill existing gaps in SERS techniques.

Keywords: MXene, SERS, quantitative analysis, superhydrophobic, flexibility.

1. Introduction

At the molecular level, achieving reliable, rapid and sensitive quantitative detection and structural identification is of paramount significance to disease diagnosis, pollution detection, food safety, analytical chemistry and many other fields(Cardinal et al. 2017; Chio et al. 2022; Homola 2008; Jeong et al. 2019; Langer et al. 2020; Zhang et al. 2021; Zhang et al. 2022). Surface-enhanced Raman scattering (SERS), as an emerging potential and powerful spectroscopy technique, can broadly detect analytes with extremely low-concentration within few seconds by identifying their unique "fingerprint" Raman information(Chio et al. 2021; Chio et al. 2020; Davison et al. 2023a; Fan et al. 2020; Lee et al. 2019; Leong et al. 2021; Li et al. 2010; Zhao et al. 2021). In SERS, the enhancement of Raman signal is considered to mainly depend on the electromagnetic (EM) enhancement caused by the local surface plasmon resonance (LSPR) of plasmonic nanoparticles (e.g., Au, Ag and Cu)(Dang et al. 2022; Davison et al. 2023b; Ding et al. 2017; Ji et al. 2022; Lombardi and Birke 2009). Notably, at the sharp vertices of plasmonic nanoparticles and the gap between adjacent nanoparticles (typically 2-10 nm), ultrasensitive plasmonic "hot spots" can be obtained(Nie and Emory 1997). However, in a highly diluted solution, the random diffusion of the analyte molecules typically sacrifices the quantitative detection capability of SERS, as the molecules at the "hot spots" contribute more to the Raman signal enhancement(Fang et al. 2008), which prevented SERS from moving towards a more accurate and dependable analytical technique.

In this context, various methods have been introduced to "enrich" analytes on SERS substrates to overcome the "dilution effects", such as adsorption concentration and analyte capture strategies(Achadu et al. 2020; Ding et al. 2020; Yang et al. 2021). Among them, the superhydrophobic platform was considered to be one of the most successful approach due to the advantages of concentrating analyte molecules to a small region and being "label-free"(Lee et al. 2013; Sahin et al. 2022; Yang et al. 2016). For instance, by silvering the surface of superhydrophobic natural taro leaves or rose petals(Chou et al. 2015; Yao et al. 2021), the detection of R6G at nanomolar concentrations can be achieved. However, the structural differences between batches of natural templates will significantly affect the sensitivity and reproducibility of SERS, making it unsuitable for quantitative detection. Moreover, the superhydrophobic substrates used are generally low SERS activity materials with enhancement signals only obtained from noble metals, missing valuable opportunities for further sensitivity improvement.

Two-dimensional metal carbides and nitrides (MXenes) have been shown to enhance Raman signals through chemical (CM) enhancement via charge transfer (CT)(Limbu et al. 2020; Sarycheva et al. 2017). Due to their tunable electronic structure, high carrier mobility, surface plasmon resonance (SPR) and other properties(El-Demellawi et al. 2018; Han et al. 2020; Jiang et al. 2020), a variety of MXenes for high-performance SERS substrates have been reported(He et al. 2022; Soundiraraju and George 2017). For example, Ta_2CT_x and Nb_2CT_x MXene can detect 10^{-9}M of SARS-CoV-2S protein(Peng et al. 2021). Highly crystalline $Ti_3C_2T_x$ MXene nanosheets have

a detection limit of 10^{-11}M for trichlorophenol(Ye et al. 2020). To further improve the SERS performance of MXene materials, emerging strategies have shifted from pure MXene to hybrid systems with precious metal nanoparticles and multidimensional plasmonic platforms, which integrate the inherent properties of both materials to overcome their respective limitations(Lee et al. 2019; Liu et al. 2021; Xie et al. 2019). For instance, we have recently prepared an ultra-sensitive SERS fiber by constructing hotspots in situ on flexible MXene-based fiber, allowing sampling and detection of explosives residues from fingerprints or sample bag surfaces(Liu et al. 2023). Although this makes SERS a widely used technology more promising, there are still many challenges. Firstly, these nanoscale hybrid substrates usually need to be deposited on the substrate or directly mixed with the analyte molecules for SERS testing, which makes the results susceptible due to the effect of "coffee ring" from water surface tension, and random diffusion of analytes. On the other hand, either MXenes or some precious metals (such as Ag) are easily oxidized and will inevitably affect the long-term stability of the SERS substrate, thereby reducing the reliability of the results. Those issues are often overlooked but are critical to practical applications. Therefore, more efforts are needed to develop a composite platform with low limit of detection (LOD) and high uniformity to balance the conflict between SERS sensitive and reproducibility.

Herein, we have built a low-cost SERS analytical platform with analyte enrichment function, which exhibits robust quantitative capability and high sensitivity for low-concentration analytes. With the help of the self-assembly properties of the two-dimensional material, the freestanding $Ti_3C_2T_x$ MXene/Au nanocubes (denoted as MXene/AuNCs) composite membranes were prepared on a large scale (~50 cm^2) by selective vacuum-assisted filtration of pure $Ti_3C_2T_x$ MXene and subsequent MXene/AuNCs hybrid colloidal solutions. The bottom side of the pure $Ti_3C_2T_x$ MXene layer endowed the membrane with excellent flexibility and low-cost fabrication, while the MXene/AuNCs layer on the upper side of membrane achieve Raman signals' enhancement from plasmonic coupling (EM) of nearby AuNCs at lateral and longitudinal direction, and improved the charge transfer (CM) capability between the $Ti_3C_2T_x$ MXene and target molecules. Furthermore, via superhydrophobic treatment by (1H,1H,2H,2H-perfluoro-octyltriethoxysilane, FOTS), the analytes can be spontaneously enriched on the surface of the membranes while protecting the SERS substrate from oxidation. Thus, the resultant MXene/AuNCs-FOTS substrate demonstrated ultralow-concentration quantitative analysis with signal uniformity and good identification capability from triple-enhancements of EM, CM and enrichment of analytes, meanwhile maintaining the stability of membrane substrate for up to several months. Moreover, as a proof-of-concept application, uric acid and xanthine biomarkers were accurately quantified in synthetic urine with an error of less than 8%. We believe that this low-cost and mass-producible SERS membrane substrate has powerful analytical capabilities and is expected to promote SERS as a broad application technology.

2. Materials and method

2.1 Materials

Ti_3AlC_2 powder was purchased from Laizhou Kaiene Ceramic Material Co., Ltd. Lithium fluoride (LiF, ≥99.0%), creatinine ($C_4H_7N_3O$, ≥99.0%), and xanthine ($C_5H_4N_4O_2$, ≥99.0%) were purchased from Macklin. 1H,1H,2H,2H-perfluoro-octyltriethoxysilane (FOTS) ($C_{14}H_{19}O_3F_{13}Si$, ≥97.0%), urea (CH_4N_2O, ≥99.0%), uric acid ($C_5H_4N_4O_3$, ≥99.0%) and rhodamine 6G (R6G, $C_{28}H_{31}N_2O_3Cl$, ≥99.0%) were purchased from Aladdin. Chloroauric acid ($HAuCl_4·4H_2O$, ≥99.99%), ascorbic acid ($C_6H_8O_6$, AA, ≥99.7%), citric acid ($C_6H_8O_7$, ≥99.0%), sodium borohydride ($NaBH_4$, ≥98%), hydrochloric acid (HCl, 36-38%), cetyltrimethylammonium chloride (CTAC) ($C_{19}H_{42}ClN$, >95%), sodium bromide (NaBr), crystal violet (CV) ($C_{25}H_{30}ClN_3$, ≥99.0%) and sodium chloride (NaCl, ≥99.9%) were purchased from Sinopharm Chemical Reagent Co., Ltd. (Shanghai, China). Deionized water (homemade) was used throughout the experiments and all chemicals were used directly without purification.

2.2 Fabrication of MXene/AuNCs Freestanding Membranes

The freestanding $Ti_3C_2T_x$ MXene/AuNCs membranes (denoted as MXene/AuNCs) were prepared by a selective vacuum-assisted filtration of pure $Ti_3C_2T_x$ MXene and MXene/AuNCs hybrid colloidal solutions in sequence, where the MXene/AuNCs hybrid was prepared by mixing 3 ml 3 mg/ml $Ti_3C_2T_x$ MXene and 50 ml 3 nM AuNCs for 12h under continually stirring at room temperature. Then the mixture was centrifuged and configured by DI water as designed.

Typically, 7 ml of $Ti_3C_2T_x$ MXene (3 mg/ml) was first filtered through a polycarbonate membrane with a pore size of 0.2 μm. Afterwards, the produced MXene/AuNCs hybrid solution was further filtered on the surface of the $Ti_3C_2T_x$ MXene membranes. Finally, after drying in a vacuum oven at 40°C for 2 h, the composite membrane was carefully peeled off from the polycarbonate membrane to obtained MXene/AuNCs membrane.

2.3 Preparation of Superhydrophobic MXene/AuNCs Membranes

MXene/AuNCs membranes were firstly treated by using oxygen plasma (FEMTO SCIENCE, CUTE-MP/R, 100 W) for 5 min. Then, the MXene/AuNCs membranes were immersed in a FOTS/ethanol solution (V_{FOTS}:$V_{ethanol}$ = 1:9) for 1 h. After that, the excess functional groups were washed away with ethanol and dried naturally at room temperature to obtain the superhydrophobic FOTS treated MXene/AuNCs membranes (noted as MXene/AuNCs-FOTS).

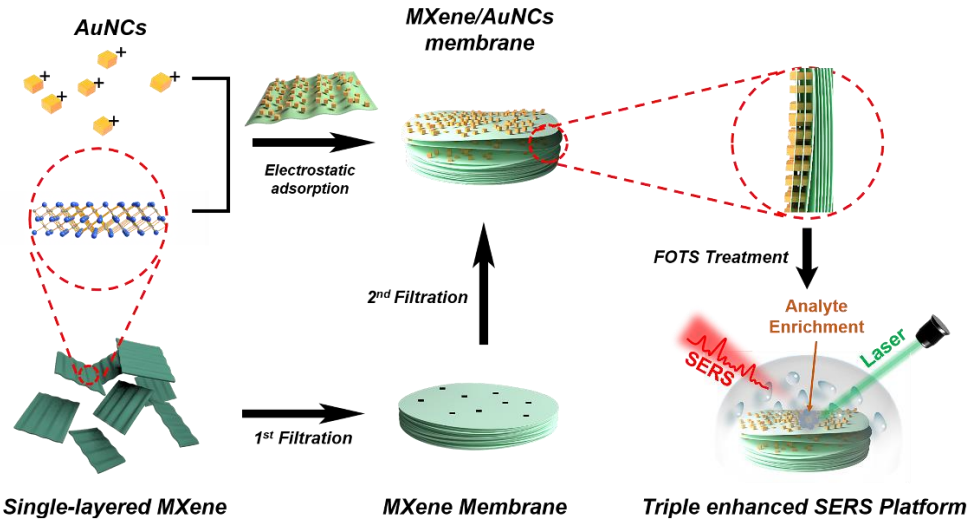

Schematic 1. Preparation process of the triple-enhanced SERS MXene/AuNCs-FOTS platform.

2.4 Synthesis of Artificial Urine

Artificial urine was synthesized based on reported work(Sarigul et al. 2019). Briefly, 166.512 mM urea, 5.194 mM creatinine, 1.633 mM citric acid and 61.745 mM sodium chloride were dissolved in deionized water. For SERS analysis of uric acid and xanthine within urine, various concentrations of uric acid and xanthine were dissolved in the artificial urine separately for the SERS measurements.

2.5 SERS experiment

To prepare the samples for SERS measurement, R6G and CV aqueous solutions were used as the probe molecules. A series of R6G and CV solutions with different concentrations from 10^{-4} M to 10^{-14} M were produced separately. Typically, 5 μl R6G/CV solutions with different concentrations were dropped onto the MXene/AuNCs-FOTS SERS substrate, and then SERS characterization was performed after drying. As the solvent evaporated, the analytes were gradually enriched on the membranes, and eventually a tiny "spot" was formed. Then, SERS spectra of samples were obtained by using an Alpha300R confocal Raman microscope (WI Tec) at an excitation wavelength of 532 nm (power = 0.1 mW). A 50× objective with 5 s acquisition time was used for data collection, and all Raman spectra were measured 3 times from at least 5 different positions of the sample. SERS mapping measurements were performed at a step of 0.7 μm. Moreover, the Raman signals of R6G/CV molecules on the $Ti_3C_2T_x$ nanosheets, AuNCs film and untreated MXene/AuNCs substrate were also conducted as references.

In the proof-of-concept experiment, the same test method and conditions were also used for the detection of different concentrations of uric acid and xanthine (from 10^{-3} M to 10^{-9} M) within artificial urine. Here the power of the laser was adjusted to 0.8 mW.

2.6 Characterization

Scanning electron microscopy (SEM, Verios G4, 5 kV) was employed to characterize the morphology and structure of samples. Transmission electron microscopy (TEM) images of $Ti_3C_2T_x$ MXene nanosheets and AuNCs were obtained by a Talos F200X microscope at 200 kV. The crystalline structures of all samples were examined and analyzed with an X-Pert PRO X-ray diffractometer (Cu Kα1, λ=0.154 nm). X-ray photoelectron spectroscopy (XPS, Thermo Scientific TM K-Alpha TM+ spectrometer, Al Kα X-ray source) was employed to characterize the valence state of each element. All peaks were calibrated with the C1 s peak binding energy at 284.8 eV for adventitious carbon. Atomic force microscopy (AFM, Dimension Icon, Bruker) was employed to measure the roughness of membranes. An optical contact angle measuring instrument (KRUSS, DSA) was used to characterize the hydrophobic properties of membranes. The absorption spectra were recorded by a Persee TU-1810PC UV–vis spectrophotometer.

3. Results and Discussion

The fabrication process of the MXene/AuNCs-FOTS membranes was illustrated in **Schematic 1**. To obtain a highly stable and sensitive SERS signal, the positively charged AuNCs modified by CTAC molecules were synthesized via the seeded-growth method (see details in the **Supporting Information**), where the synthesized AuNCs are nearly monodisperse with an average edge length of 66.8±5.4 nm (**Figure 1a** and **Figure S1a**). Furthermore, the single crystalline AuNCs are formed and grew along the (200) crystal plane, as illustrated in the electron diffraction spectrum at insert in **Figure 1a**. Moreover, the UV-vis absorption peak of the AuNCs colloidal solution was located at 562 nm (**Figure S1b**) and expected to exhibit a strong and distinct localized surface plasmon resonance (LSPR) to enhance the Raman signal of target molecules. In preparing a freestanding MXene membrane, single-layer or few-layers $Ti_3C_2T_x$ MXene nanosheets (**Figure 1b**) with a lateral size of approximately 300 nm were prepared by selective etching method (see details in the **Supporting Information**). Typically, Al layers of Ti_3AlC_2 powders were etched away by LiF/HCl mixed solution and left abundant hydroxyl (−OH), oxygen (−O), and fluorine (−F) groups on the surface of $Ti_3C_2T_x$ MXene nanosheets, which cannot only bind to AuNCs by electrostatic adsorption but can also be used as a covalent attachment site for surface functionalization(Chen et al. 2020).

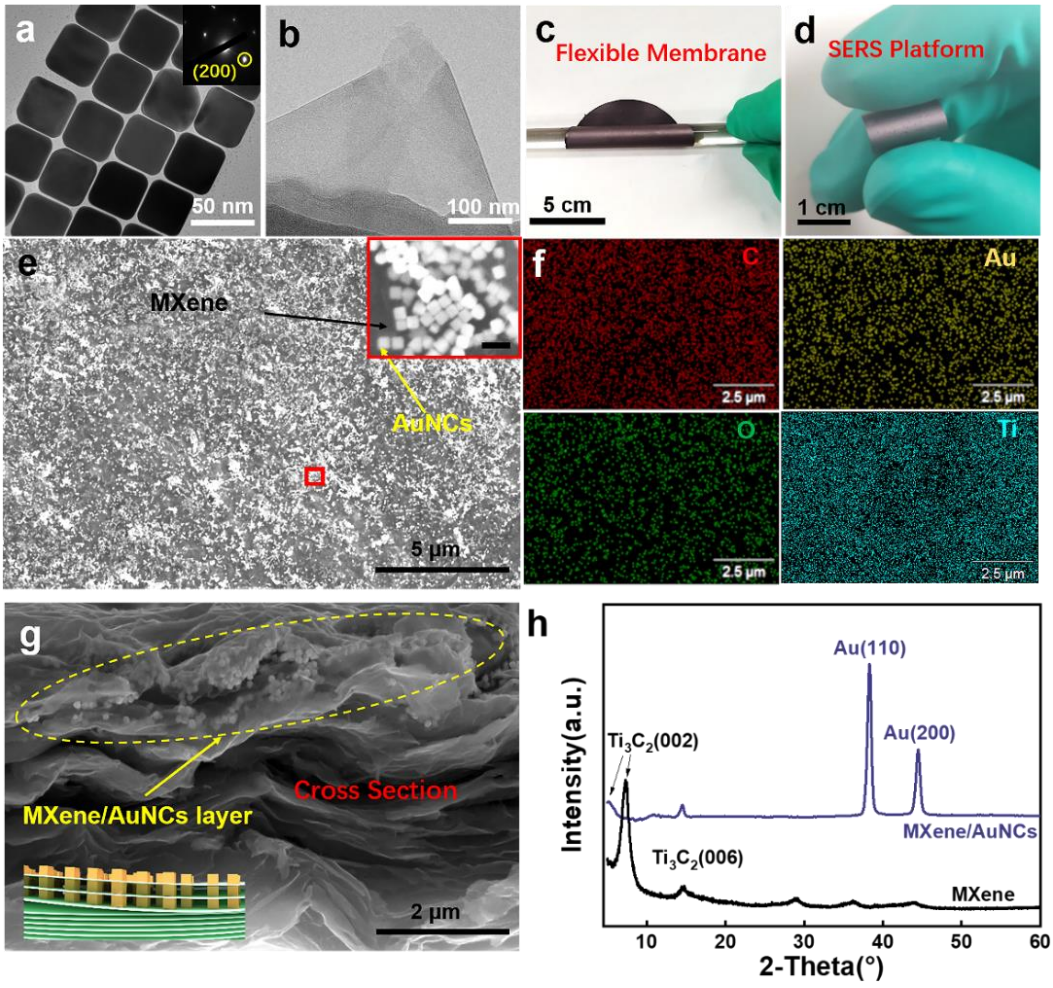

Figure 1. (a) and (b) HR-TEM images of AuNCs and $Ti_3C_2T_x$ MXene nanosheets. Inset in (a) is the corresponding electron diffraction image of AuNCs. (c) and (d) Optical photos of the free-standing flexible $Ti_3C_2T_x$ MXene and MXene/AuNCs membranes. (e) SEM image of the top view of MXene/AuNCs membrane and (f) its corresponding EDS mapping of C, O, Au and Ti elements. Inset in (e): the high magnification of (e). (g) SEM image of a cross section of MXene/AuNCs membrane, and the schematic of structure of top layer of MXene/AuNCs, as circled by the yellow dashed line. (h) XRD patterns of the $Ti_3C_2T_x$ MXene and MXene/AuNCs membranes.

The freestanding MXene membrane with excellent flexibility ~50 cm^2 (**Figure 1c**) was fabricated by filtering 7 mL of 3 mg/mL $Ti_3C_2T_x$ MXene aqueous solution through a pore size of 0.2 μm polycarbonate membrane. After the formation of a stable $Ti_3C_2T_x$ MXene membrane, a MXene/AuNCs hybrid colloidal solution was further deposited on the surface of the $Ti_3C_2T_x$ MXene membrane to construct MXene/AuNCs membrane substrate (**Schematic 1**). Under the dual effects of selective vacuum-assisted filtration and electrostatic adsorption, AuNCs were not only anchored on the surface of the $Ti_3C_2T_x$ MXene membrane but also incorporated in the upper layer of MXene/AuNCs membrane, and thus the corresponding color of the membrane gradually became more metallic luster (**Figure 1d** and **e**).

SEM images confirmed that AuNCs were not only uniformly and densely anchored on the surface of membrane (**Figure 1f**), but also incorporated in between of MXene nansheets on the upper layer of the MXene/AuNCs membrane (**Figure 1g**). The formed structure could provide a strong electric field from the plasmon coupling of nearby AuNCs at lateral and longitudinal direction (**Figure 1 e** and **g**) of membrane substrate. The energy dispersive X-ray spectroscopy (EDS) mappings of MXene/AuNCs membrane clearly show a uniform distribution of C, Ti, O and Au (**Figure 1f**), which was crucial for the superhydrophobic treatment and the signal uniformity of SERS. Furthermore, the bottom layer from first filtration of $Ti_3C_2T_x$ MXene has a typical anisotropic characteristics as the upper layer of MXene/AuNCs of membrane (**Figure S2**), endowing with its excellent mechanical performance (Cao et al. 2020) . The structures of $Ti_3C_2T_x$ MXene and MXene/AuNCs membranes were further characterized by XRD, as shown in **Figure 1h**. The sharp peak near 7° proves the successful synthesis of $Ti_3C_2T_x$ MXene, and the diffraction peak at 44.25° corresponds to the (200) crystal plane of Au, which verifies the previous result of electron diffraction in **Figure 1a**. Moreover, the (002) peak of $Ti_3C_2T_x$ MXene after being compounded with AuNCs downshifts from 7° to 5.9°, indicating an increase in the interplanar distance due to the incorporation of CTAC-grafted AuNCs. The grafted CTAC molecules on the AuNCs surface can improve the charge transfer of $Ti_3C_2T_x$ with target molecules, which may increase the SERS signal strength(Wang et al. 2021a).

One of the most important parts of SERS to achieve ultralow concentration detection is to enrich the analyte concentration on the detection location. Since the contact angle of the analyte solution at surface of the superhydrophobic substrate almost remains unchanged during the drying process, the analyte will be enriched into a smaller area and the corresponding detection limit of SERS increased (Lee et al. 2013; Liu et al. 2020; Sahin et al. 2022). Here, 1H,1H,2H,2H-perfluoro-octyltriethoxysilane (FOTS) molecules were used to modify the wettability of the MXene/AuNCs

membrane substrate (see details in the **Experimental Section**). As demonstrated in **Figure 2a**, the contact angle (CA, θ) of pure $Ti_3C_2T_x$ MXene membrane showed a typical hydrophilicity, where the CA of substrate is around 48° attributing to the existence of the hydrophilic group of −OH and −O. In contrast, the CA of the FOTS treated $Ti_3C_2T_x$ MXene substrate increased to 113°, indicating FOTS molecules could be substantially reduced the surface energy of the membrane due to the low surface energy of –F group augmented. In addition, the oxidation of $Ti_3C_2T_x$ MXenes is usually caused by contact with moisture in the air, so superhydrophobic treatment may increase the shelf life of the substrate (Wang et al. 2021b).

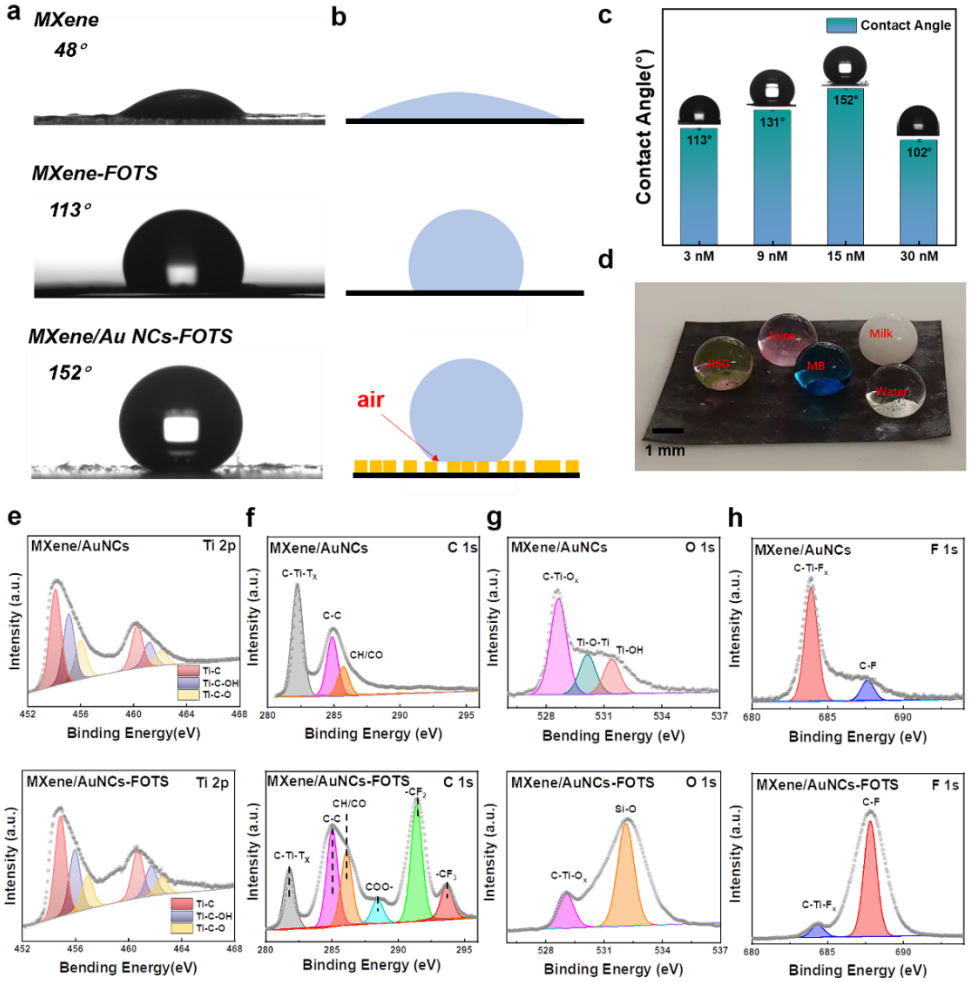

Figure 2. (a) Digital images of water contact angle (CA) measurements of $Ti_3C_2T_x$ MXene, $Ti_3C_2T_x$ MXene-FOTS, and MXene/AuNCs-FOTS membranes and (b) their respective models. (c) Relationship between the CA and the contents of AuNCs within the MXene/AuNCs-FOTS membranes. (d) Photographs of different types of liquids dripping on the surface of the MXene/AuNCs-FOTS membranes. XPS spectra of (e) Ti 2p, (f) C 1 s, (g) O 1 s and (h) F 1 s elements within MXene/AuNCs (top row) and MXene/AuNCs-FOTS (bottom row) membranes.

According to the Cassie model (**Figure 2b**), the introduction of AuNCs and subsequent FOTS treatment (noted as MXene/AuNCs-FOTS), the surface roughness of membrane substantially increased, leading to the formation of air cushions when the droplets come into contact with the membrane. Thereby, MXene/AuNCs-FOTS membrane substrate demonstrates a much higher CA (θ > 150°), where the formed

superhydrophobic membrane could have a great potential for using an ultralow detection of SERS analysis platform. Moreover, to achieve the best superhydrophobic performance, the surface roughness of MXene/AuNCs-FOTS was mediated by the variation of AuNCs contents (3 nM, 9 nM, 15 nM and 30 nM) within the MXene/AuNCs hybrids solutions. The SEM and 3D AFM images clearly show the distributions of AuNCs on the surface of MXene membranes. As demonstrated in Figure **S3** and **S4**, as the AuNCs contents increased from 3 nM to 15 nM, the surface roughness (Rq) of MXene/AuNCs-FOTS changed from 93 nm to 156 nm due to the increase in AuNCs density (**Figure S3a-c** and **Figure S4a-c**), thus their corresponding CA gradually increased from 113° to 152°. However, with the further increase of AuNCs content to 30 nM, the surface roughness reduced to 87 nm (**Figure S4d**) because of the aggregation of excess AuNCs on the surface of MXene/AuNCs membrane (**Figure 2c and Figure S3d**), which subsequently reduced the CA to 102°. Based on the above results, the contents of AuNCs within hybrids of 15 nM was considered to be the most optimized value for improving the surface superhydrophobic performance of membrane. In addition, MXene/AuNCs-FOTS membrane also have a strong repellent effect on other common liquids for a range of applications, including body fluid detection (**Figure 2d**).

To reveal the changes in surface energy and bonding configurations of MXene/AuNCs before and after FOTS treatment, X-ray photoelectron spectroscopy (XPS) was used to record the state of elements (**Figure 2e-h**). The Ti 2p spectrum in **Figure 2e** was fitted with Ti-C, Ti-C-OH and Ti-C-O peaks,(Choi et al. 2020) and the positions and the intensities of those three peaks in MXene/AuNCs showed almost no change after FOTS treatment, confirming that Ti 2p was mostly not reacted with the FOTS molecules. Comparing with C1s spectra of untreated MXene/AuNCs, two new peaks at 291.0 eV and 293.2 eV appeared, which are mainly attributed to $–CF_2$ and $–CF_3$, respectively (**Figure 2f**). From the calculation of these two fitted peak areas, the ratio of $–CF_2/–CF_3$ was approximately to 5.21 that closely resembles to the theoretical molecular structure of FOTS, verifying successful modification by FOTS. The O 1 s spectra suggested that the untreated MXene/AuNCs membrane had abundant amounts of -O and -OH functional groups, corresponding to the peaks at 530.4 eV and 531.7 eV, respectively (**Figure 2g**). After treatment with FOTS, an intense Si-O peak at 532.9 eV suggested that FOTS was grafted on the membrane by interaction with the oxygen-containing functional groups on $Ti_3C_2T_x$ MXene, which was consistent with the results of infrared spectroscopy (**Figure S5**). The C-F and C-Ti-F peaks at 687.6 eV and 683.9 eV appeared of F1s spectra (**Figure 2h**) for both of untreated and treated MXene/AuNCs membranes. However, the C-F/C-Ti-F content of treated MXene/AuNCs by FOTS molecules increased significantly, suggesting that C-F bonds were introduced in large numbers.

The “coffee ring” effect is a ubiquitous phenomenon during analytes solution evaporation, which hinders the quantitative detection of SERS at ultralow concentrations due to the inhomogeneous distribution of molecules on the substrate (Yunker et al. 2011). When the droplet containing the analyte comes into contact with the hydrophilic surface, the three-phase contact line between atmosphere, droplet and

solid substrate has been fixed and Marangoni flow occurs during the solvent evaporation. It drives the solute outwards from the inside to the edge of the droplet, and finally a ring-shaped spot is left on the surface of the MXene/AuNCs membranes (**Figure 3 a_1~a_3**). Most of the molecules of the analyte will be concentrated on the ring, causing the signal deviation of the SERS at different positions. In contrast, when the analyte droplet dries on the FOTS-treated surface with superhydrophobic property, the analyte will always leave a uniform spot on the MXene/AuNCs-FOTS membranes due to the constant contact angle or/and the gradually increasing viscosity that suppresses the Marangoni flow during the solvent evaporation (Hu and Larson 2006; Seo et al. 2017) (**Figure 3 b_1~b_3**). To quantify the "coffee ring" effect on the SERS performance of substrate, R6G (1×10^{-10} M, 5 μl) aqueous solutions were used as probe molecules and dropped on the surface of MXene/AuNCs and MXene/AuNCs-FOTS membranes. After complete drying, the 612 cm^{-1} peak of R6G was used to perform SERS mapping on the measured area. As shown in **Figure 3 a_4** and **b_4**, MXene/AuNCs-FOTS membrane showed a more uniform SERS signal than MXene/AuNCs substrate. Furthermore, SERS spectra of R6G were collected from 10 randomly selected regions in both substrates, and the relative standard deviation (RSD) at 612 cm^{-1} was calculated (**Figure 3a_5, b_5** and **c**). Obviously, the RSD (6.41%) of MXene/AuNCs-FOTS is much lower than that of MXene/AuNCs (51.94%) and previous work as well (Cao et al. 2020; Liu et al. 2021; Xie et al. 2019; Yao et al. 2021) (**Table S1**).

In addition, in **Figure 3d**, the SERS spectra of R6G collected from MXene/AuNCs-FOTS membrane show the minor changes after storage in air for over 90 days. Moreover, by monitoring the variations of Raman peak intensity of R6G in 612 cm^{-1} over time, it was found that after 90 days of storage, the MXene/AuNCs-FOTS membrane retained 83.7% of the signal intensity, whereas the MXene/AuNCs membrane decreased to 52.3% of the initial intensity (**Figure 3e** and **Figure S6**). These results indicate that FOTS functionalization exhibits a significantly improved environmental stability and provides a solution to overcome the oxidation tendency of $Ti_3C_2T_x$ MXene in a humid environment, thus increases the shelf-life of the substrate. For further confirmation, the XRD patterns of MXene/AuNCs and MXene/AuNCs-FOTS membranes at different storage time in a humid atmosphere are shown in **Figure S7**. For MXene/AuNCs, a new peak appears at 25.1° after 90 days storage, which can be ascribed to the formation of TiO_2. In contrast, there was no prominent difference in the MXene/AuNCs-FOTS after the humid treatment.

On the other hand, the analyte enrichment effect due to the superhydrophobic treatment was also quantified. As shown in **Figure 3f**, a functional relationship between the droplet contact angle and contact area on the membranes surface was obtained by constructing a typical analytical model (see details in the **Supporting Information**). According to the calculations, the contact areas of 5 μl droplets on MXene/AuNCs-FOTS and MXene/AuNCs are 5.2 mm^2 and 12.6 mm^2 respectively, which suggests that the analytes in the droplet will be enriched in a much smaller area, thus more than doubling the detection limit of the MXene/AuNCs-FOTS substrate can be obtained (**Figure 3g**). In fact, during the actual drying process, the contact area of the superhydrophobic surface gradually decreased with the evaporation process, and the

pinning effect only occurs after the droplet shrinks to a certain size, thus the enrichment of analytes in the actual process can be realized. For further proof, SERS spectra of 10^{-10} M R6G were collected from the MXene/AuNCs-FOTS and MXene/AuNCs membranes. As shown in **Figure S8**, a stronger R6G signals was obtained after the superhydrophobic treatment, which supports the above conclusions. These exciting results confirm that the FOTS with low surface energy treated MXene/AuNCs membrane provides an approach to overcome the temporal and spatial instability of Raman signals and clear the way for low-concentration quantitative analysis of SERS.

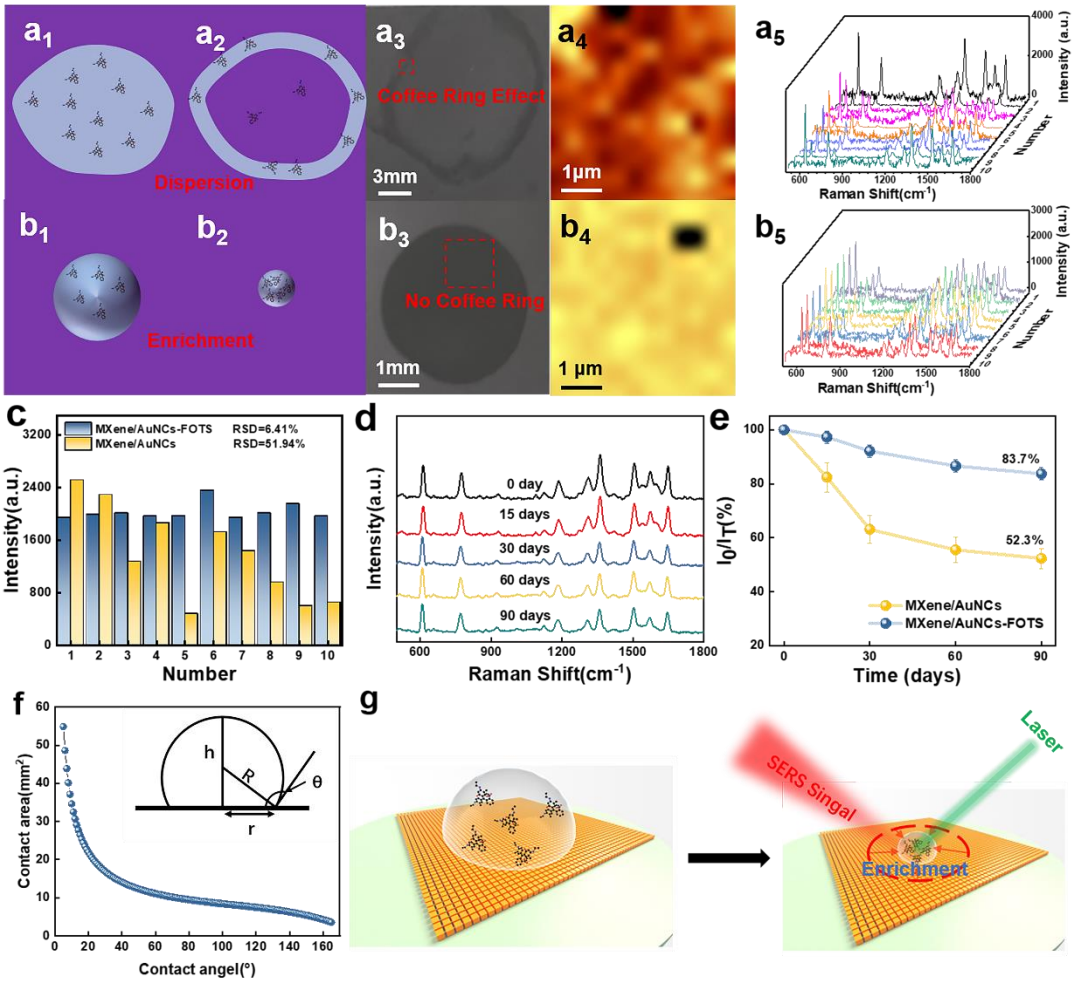

Figure 3. Comparison of SERS reliability and stability of MXene/AuNCs and MXene/AuNCs-FOTS membranes. (a_1) ~(a_3) and (b_1) ~(b_3) Drying process of 1×10^{-10} M R6G aqueous droplets on the surface of MXene/AuNCs and MXene/AuNCs-FOTS membranes, respectively, and (a_4) and (b_4) the corresponding Raman mapping of the 612 cm^{-1} characteristic peak of R6G. (a_5) and (b_5) SERS spectra of R6G collected from 10 randomly selected regions of MXene/AuNCs and MXene/AuNCs-FOTS membranes. (c) RSD value of MXene/AuNCs and MXene/AuNCs-FOTS membranes calculated from peak intensities at 612 cm^{-1}. (d) SERS spectra of R6G collected from MXene/AuNCs-FOTS membranes after storage in air for various times. (e) Attenuation of Raman signal intensity versus storage time before and after the superhydrophobic treatment. (f) Contact area of 5 μL analyte solution on the SERS platform as a function of the CA. Insert in (f): model for calculation. (g) Schematic of the variation of concentration of analyte solution with the evaporation of solvent.

The commonly used SERS probes R6G and CV were used to evaluate the SERS sensitivity of MXene/AuNCs-FOTS membrane substrate and its low concentration quantification capability. **Figure 4a and 4b** shows the Raman spectra of 10^{-8}~10^{-14} M R6G and 10^{-8}~10^{-12} CV molecules on the surface of MXene/AuNCs-FOTS, and the characteristic peaks can be clearly observed at each concentration due to the enrichment effect of the superhydrophobic treatment and the dense plasmonic hotspots. The Raman enhancement factor (EF) of MXene/AuNCs-FOTS membrane is calculated to be approximately 3.19×10^{9} (see details in **Supporting Information**), which is much better than most MXene and precious metal particle analysis platforms (Fan et al. 2013; He et al. 2022; Liu et al. 2021; Peng et al. 2021; Soundiraraju and George 2017; Xie et al. 2019). This excellent property was largely attributed to triple-enhanced effect, including EM from the plasmonic coupling of nearby AuNCs at lateral and longitudinal direction, the improved CM effect from the charge transfer capability between the $Ti_3C_2T_x$ MXene and target molecules and the enrichment of the analytes by the superhydrophobic MXene/AuNCs-FOTS platform. In addition, the SERS intensities of the 612 cm^{-1} and 1618 cm^{-1} peaks of R6G and CV were used for polynomial fitting, respectively. As shown in **Figure 4c**, the characteristic peak Raman intensity correlates well with the logarithm of the probe molecule concentration, implying its potential in quantitative analysis at low concentrations. Interestingly, when the concentration of the molecules falls below 10^{-11} M, the decrease in concentration leads to a relatively small deviation in signal intensity for R6G due to the physical adsorption of molecules on sensor can be approximated as a Langmuir isotherm (above this concentration, it becomes multilayer adsorption), where the formed monolayer or sub-monolayer molecules absorbed on the substrate. Thus, the number of excited molecules does not change much with concentrations, resulting in a smaller signal change (Lee et al. 2013).

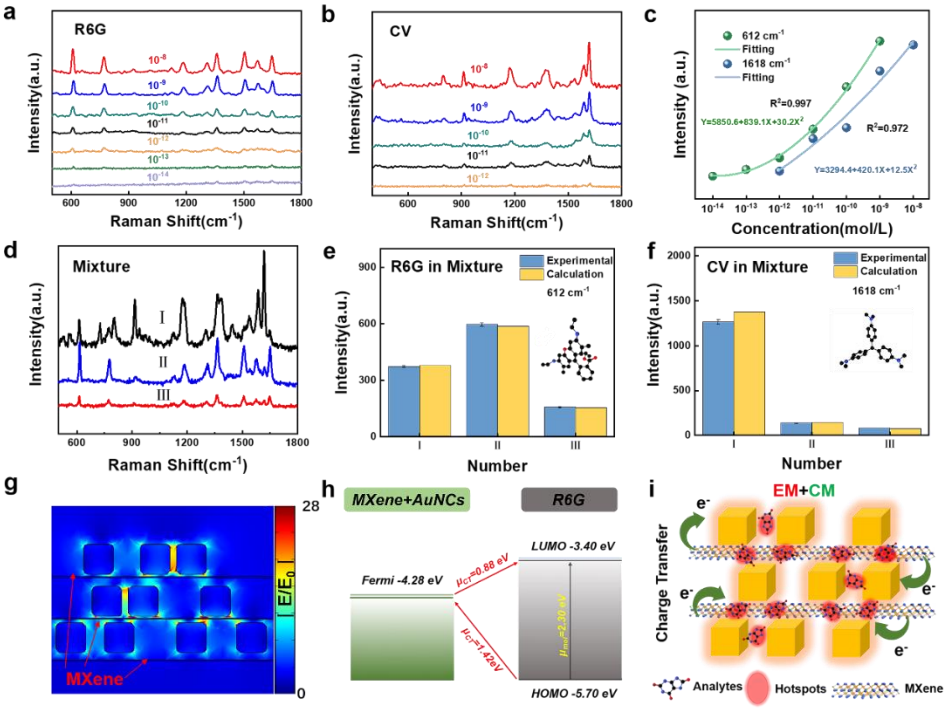

Figure 4. SERS performance and triple enhancement mechanism of MXene/AuNCs-FOTS platform. (a) and (b) SERS spectra of R6G and CV molecules with different concentrations collected from MXene/AuNCs-FOTS membrane substrate. (c) Raman intensities at 612 cm^{-1} peak for R6G and 1618 cm^{-1} peak for CV from (a) and (b) as functions of the concentrations and their corresponding fitting lines. (d) SERS spectra of three mixtures, such as I from 5×10^{-11}M R6G mixed with 5×10^{-6} M CV, II from 1×10^{-11} M R6G mixed with 2×10^{-11} M CV, and III from 1×10^{-12} R6G mixed with 5×10^{-12} M CV. (e) R6G and (f) CV were successfully predicted through comparative experiments and calculations. (g) Electric field distribution of AuNCs on the cross section of MXene/AuNCs-FOTS membrane substrate. (h) Charge-transfer process between R6G and the SERS substrate. (i) Schematic illustration of the analytes detection process on MXene/AuNCs-FOTS membrane.

As a further verification, MXene/AuNCs-FOTS membrane was used to identify the respective concentrations of R6G and CV in mixed solutions. As shown in **Figure 4d**, complex SERS spectra composed of R6G and CV were observed from all mixtures. Through a detailed comparison of actual measured and calculated values based on the calibration curves in **Figure 4c** (see details in **Figure 4e, 4f** and **Table S2**), the respective concentrations of R6G and CV were quantified by the 612 cm^{-1} and 1618 cm^{-1} peaks. Thus, the MXene/AuNCs-FOTS membrane demonstrates a great value for quantitative analysis for target molecules with low-concentration.

Furthermore, the underlying Raman enhancement mechanisms of the substrate were investigated theoretically and experimentally. First, the SERS performance of the $Ti_3C_2T_x$ MXene nanosheets, AuNCs and MXene/AuNCs-FOTS membrane substrates was investigated (**Figure S9**), where the $Ti_3C_2T_x$ MXene and AuNCs (**Figure S10**) were deposited on quartz flakes for the Raman measurements respectively (see details in the **Experimental Section**). Although Raman-enhanced spectra for R6G can be obtained from different substrates, the strongest Raman intensity was obtained when the probe molecules placed on the MXene/AuNCs-FOTS, suggesting the SERS behavior of molecules is mainly dominated by a combination of LSPR-induced electromagnetic field enhancement and interfacial CT effects (Ding et al. 2017; Limbu et al. 2020; Lombardi and Birke 2009). UV–vis absorption spectra showed strong absorption peaks at 562 nm and 785 nm for AuNCs and $Ti_3C_2T_x$ MXene, respectively (**Figure S1b** and **S11**). These significant absorption peaks can be reasonably attributed to the abundance of outermost orbital free electrons of AuNCs and $Ti_3C_2T_x$ MXene, implying a strong LSPR for both (El-Demellawi et al. 2018). Then, the distribution and intensity of the electromagnetic field on the surface and cross section of the upper layer of MXene/AuNCs membrane substrate was calculated by the finite element method (FEM, see detail in **Supporting Information**). As shown in **Figures 4g** and **S12**, under laser excitation at 532 nm, the electromagnetic field generated by the coupling between $Ti_3C_2T_x$ MXene and AuNCs in the lateral direction along with the surface of membrane is stronger than that of AuNCs alone, and the maximum value of $|E/E_0|$ can reach 27.9. Moreover, the plasmonic coupling of AuNCs to $Ti_3C_2T_x$ MXene in the longitudinal direction also generates dense hot spots (**Figure 4g and i**). The above results demonstrate that the produced membrane substrate can generate a strong local electromagnetic field to induce Raman signal enhancement.

In addition to the electromagnetic enhancement mechanism, the photo-induced charge transfer (PICT) between the substrate and the analyte is another important SERS enhancement mechanism (Lombardi and Birke 2009). In general, the enhancement of the Raman signal is proportional to the square of the molecular polarization tensor (α), α=A+B+C, where the A term represents the contributions from the electromagnetic fields, and the B and C terms represent the Herzberg−Teller contributions and are related to the CT transitions between substrate-to-molecule or molecule-to-substrate. Therefore, ultraviolet photoelectron spectroscopy (UPS) was used to calculate the Fermi level positions of the MXene/AuNCs-FOTS membrane to investigate possible charge transitions. As shown in **Figures 4h** and **S13**, the Fermi energy level of the MXene/AuNCs-FOTS membrane is located at -4.28 eV, while the energy levels of the lowest unoccupied molecule orbital (LUMO) and the highest occupied molecule orbital (HOMO) of R6G are -3.40 eV and -5.70 eV, respectively. This means that the energy required for PICT (μ_{CT}) to occur is only 0.88 eV and 1.42 eV, which can be easily excited by the 532 nm (2.32 eV) laser. In addition, the transition energy (μ_{mol}) from the HOMO to the LUMO of R6G was close to the excitation energy. Thus, according to the Herzberg–Teller coupling law, these PICT resonances further enhance the Raman signal through the CM mechanism. Finally, as previously mentioned, the EF of the substrate was further increased more than twofold by the enrichment of the analytes. Based on the above research, the excellent SERS performance of MXene/AuNCs-FOTS membrane substrate was considered to be dominated by a triple-enhanced mechanism (**Figure 4i**), which provides a new avenue for the design of high-performance SERS substrates.

To verify the reliability of the MXene/AuNCs-FOTS SERS substrate in actual health monitoring, two molecules (uric acid and xanthine) commonly found in urine were tested. Uric acid has been identified as one of the biomarkers for cardiovascular disease and gout (Au - Chio et al. 2020), while elevated xanthine levels can trigger kidney diseases (Westley et al. 2017). Here, a series of standard SERS spectra of uric acid and xanthine solutions with different concentrations were obtained on MXene/AuNCs-FOTS SERS substrate and are shown in **Figure 5a** and **b**. Impressively, the limit of detection (LOD) was down to 10^{-8} M for uric acid and 10^{-7} M for xanthine due to the triple enhancement mechanisms. Those values are much lower than traditional chromatography (~0.1 μg/L) and other SERS substrates (**Table S3**). Considering the shorter analysis time (~15 s), SERS detection has a good potential in the application of disease diagnosis. Moreover, the characteristic peak intensity and concentration logarithm of uric acid (1578 cm^{-1}) and xanthine (1033 cm^{-1}) were fitted by the main peak analysis method. The results are shown in **Figure S14**. The characteristic peak intensity is highly correlated with the concentration logarithm (R^2=0.97 and 0.98, respectively), indicating the potential of the MXene/AuNCs-FOTS substrate for the quantitative detection of biomarkers.

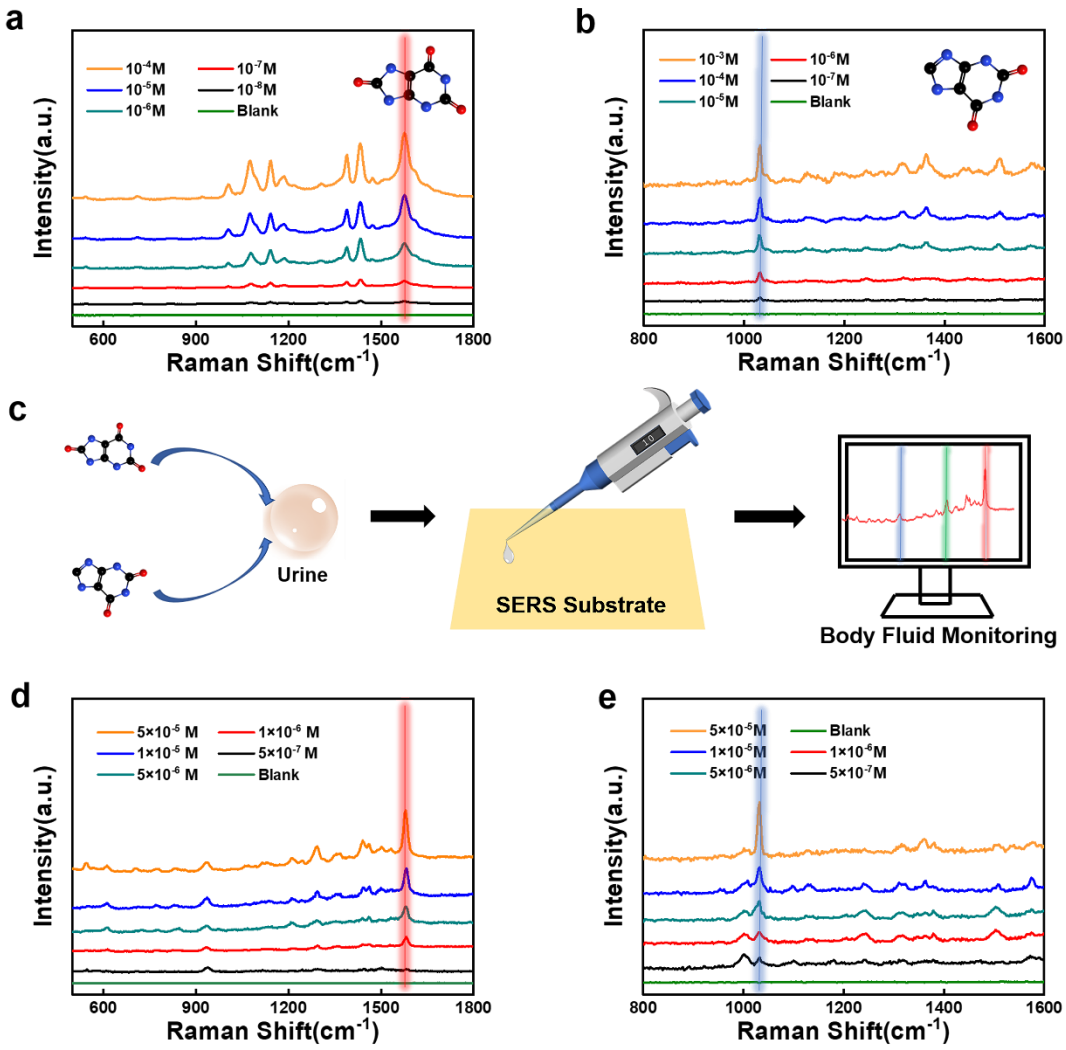

Figure 5. SERS detection of low concentration uric acid and xanthine in urine at MXene/AuNCs-FOTS platform. (a) and (b) SERS spectra of different concentrations of uric acid (left) and xanthine (right) collected from MXene/AuNCs-FOTS membranes. (Inset: structure of uric acid and xanthine). (c) Proof-of-concept schematic for detecting biomarkers in urine with high sensitivity and reliability. (d) and (e) SERS spectra of different concentrations of uric acid (left) and xanthine (right) in artificial urine collected from MXene/AuNCs-FOTS membranes.

Furthermore, a series of different concentrations of uric acid and xanthine were added to artificial urine to verify the feasibility (**Figure 5c**). The SERS signals collected from the MXene/AuNCs-FOTS substrate are shown in **Figure 5d** and **e**, and the characteristic peaks of uric acid and xanthine can be clearly distinguished from the background, even as low as 5×10^{-7} M. Here, the normal levels in human urine are 3×10^{-3} M~8×10^{-4} M and 4×10^{-4} M~1×10^{-4} M, respectively. Meanwhile, by substituting the characteristic peak intensity into the linear function curve, the error between the deduced concentration and the actual dose was also less than 8% (**Table S4**). Notably, the peaks of both biomarkers have redshifts of several wavenumbers, which are related to the change in the solution environment of the molecules (He et al. 2022; Lombardi and Birke 2009). The above demonstration shows that biomarker content-based diagnosis and screening can be performed quickly and accurately with the help of

MXene/AuNCs-FOTS SERS substrates, thus providing great value for health monitoring.

4. Conclusion

In conclusion, we have demonstrated a SERS platform with high sensitivity and reliability for ultralow-concentration quantitative detection. As proven by the experiments and theoretical simulations, the MXene/AuNCs layer located at the upper layer of the free-standing membrane generates strong plasmonic coupling in the lateral and longitudinal directions, and enhances the charge transfer (CT) between the MXene and target molecules. Moreover, the superhydrophobic treatment of the MXene/AuNCs removes the “coffee ring” effect and enriches the target analytes from the drying process, which plays a key role in enhancing the stability and sensitivity of the SERS substrate. Therefore, membranes exhibit excellent sensing performance driven by a combination of plasmonic coupling, CT and analyte enrichment. Moreover, the fabricated biosensors were used to perform proof-of-concept experiments for the detection of uric acid and xanthine in the artificial urine samples. In the future, we expect to drive SERS technology toward accurate and rapid health monitoring applications by integrating signal transmission devices and smart blocks.

Declaration of competing interest

There are no conflicts to declare.

CRediT authorship contribution statement

Xin Liu: Conceptualization, Methodology, Data curation, SERS analysis, FEM simulations, Writing – original draft. **Alei Dang:** Conceptualization, Supervision, Funding acquisition, Writing – review & editing. **Tiehu Li:** Supervision, Funding acquisition. **Yiting Sun:** Methodology. **Yuhui Liu:** FEM simulations. **Fei Ye:** Methodology. **Tung-Chun Lee:** Writing – review & editing. **Shuze Ma:** Validation. **Yong Yang:** Writing – review & editing. **Weibin Deng:** SERS analysis.

Acknowledgments

We acknowledge support by the National Natural Science Foundation of China (52072302, 51802267, 51872235), the Science and Technology Plan Project from Xi'an (22GXFW0135), the China Postdoctoral Science Foundation (2020M673475), and the Fundamental Research Funds for the Central Universities (23GH0501104).

Appendix A. Supporting Information

The following is the Supporting Information to this article:

Multimedia component 1.

Data availability

Data will be made available on reasonable request.

References

Achadu, O.J., Abe, F., Suzuki, T., Park, E.Y., 2020. ACS Applied Materials & Interfaces 12(39), 43522-43534.https://doi.org/10.1021/acsami.0c14729

Au - Chio, W.-I.K., Au - Davison, G., Au - Jones, T., Au - Liu, J., Au - Parkin, I.P., Au - Lee, T.-C., 2020. JoVE(164), e61682.https://doi.org/doi:10.3791/61682

Cao, Z., He, P., Huang, T., Yang, S., Han, S., Wang, X., Ding, G., 2020. Chemistry of Materials 32(9), 3813-3822.https://doi.org/10.1021/acs.chemmater.9b05293

Cardinal, M.F., Vander Ende, E., Hackler, R.A., McAnally, M.O., Stair, P.C., Schatz, G.C., Van Duyne, R.P., 2017. Chemical Society Reviews 46(13), 3886-3903.https://doi.org/10.1039/C7CS00207F

Chen, W.Y., Lai, S.-N., Yen, C.-C., Jiang, X., Peroulis, D., Stanciu, L.A., 2020. ACS Nano 14(9), 11490-11501.https://doi.org/10.1021/acsnano.0c03896

Chio, W.-I.K., Liu, J., Jones, T., Perumal, J., Dinish, U.S., Parkin, I.P., Olivo, M., Lee, T.-C., 2021. Journal of Materials Chemistry C 9(37), 12624-12632.https://doi.org/10.1039/D1TC02004H

Chio, W.-I.K., Moorthy, S., Perumal, J., U. S, D., Parkin, I.P., Olivo, M., Lee, T.-C., 2020. Journal of Materials Chemistry C 8(21), 7051-7058.https://doi.org/10.1039/D0TC00931H

Chio, W.-I.K., Xie, H., Zhang, Y., Lan, Y., Lee, T.-C., 2022. TrAC Trends in Analytical Chemistry 146, 116485.https://doi.org/https://doi.org/10.1016/j.trac.2021.116485

Choi, J., Kim, Y.-J., Cho, S.-Y., Park, K., Kang, H., Kim, S.J., Jung, H.-T., 2020. Advanced Functional Materials 30(40), 2003998.https://doi.org/https://doi.org/10.1002/adfm.202003998

Chou, S.-Y., Yu, C.-C., Yen, Y.-T., Lin, K.-T., Chen, H.-L., Su, W.-F., 2015. Analytical Chemistry 87(12), 6017-6024.https://doi.org/10.1021/acs.analchem.5b00551

Dang, A., Wang, Y., Zhang, H., Panatdasirisuk, W., Xia, Y., Wang, Z., Jariwala, D., Li, T., Yang, S., 2022. ACS Applied Nano Materials 5(5), 6650-6658.https://doi.org/10.1021/acsanm.2c00689

Davison, G., Jones, T., Liu, J., Kim, J., Yin, Y., Kim, D., Chio, W.-I.K., Parkin, I.P., Jeong, H.-H., Lee, T.-C., 2023a. Advanced Materials Technologies 8(7), 2201400.https://doi.org/https://doi.org/10.1002/admt.202201400

Davison, G., Yin, Y., Jones, T., Parkin, I.P., Peveler, W.J., Lee, T.-C., 2023b. Journal of Materials Chemistry C 11(9), 3334-3341.https://doi.org/10.1039/D2TC05069B

Ding, Q., Wang, J., Chen, X., Liu, H., Li, Q., Wang, Y., Yang, S., 2020. Nano Letters 20(10), 7304-7312.https://doi.org/10.1021/acs.nanolett.0c02683

Ding, S.-Y., You, E.-M., Tian, Z.-Q., Moskovits, M., 2017. Chemical Society Reviews 46(13), 4042-4076.https://doi.org/10.1039/C7CS00238F

El-Demellawi, J.K., Lopatin, S., Yin, J., Mohammed, O.F., Alshareef, H.N., 2018. ACS Nano 12(8), 8485-8493.https://doi.org/10.1021/acsnano.8b04029

Fan, M., Andrade, G.F.S., Brolo, A.G., 2020. Analytica Chimica Acta 1097, 1-29.https://doi.org/https://doi.org/10.1016/j.aca.2019.11.049

Fan, Z., Kanchanapally, R., Ray, P.C., 2013. The Journal of Physical Chemistry Letters 4(21), 3813-3818.https://doi.org/10.1021/jz4020597

Fang, Y., Seong, N.-H., Dlott, D.D., 2008. Science 321(5887), 388-392.https://doi.org/10.1126/science.1159499

Han, M., Maleski, K., Shuck, C.E., Yang, Y., Glazar, J.T., Foucher, A.C., Hantanasirisakul, K., Sarycheva, A., Frey, N.C., May, S.J., Shenoy, V.B., Stach, E.A., Gogotsi, Y., 2020. Journal of the American Chemical Society 142(45), 19110-19118.https://doi.org/10.1021/jacs.0c07395

He, Z., Rong, T., Li, Y., Ma, J., Li, Q., Wu, F., Wang, Y., Wang, F., 2022. ACS Nano 16(3), 4072-4083.https://doi.org/10.1021/acsnano.1c09736
Homola, J., 2008. Chemical Reviews 108(2), 462-493.https://doi.org/10.1021/cr068107d
Hu, H., Larson, R.G., 2006. The Journal of Physical Chemistry B 110(14), 7090-7094.https://doi.org/10.1021/jp0609232
Jeong, H.-H., Choi, E., Ellis, E., Lee, T.-C., 2019. Journal of Materials Chemistry B 7(22), 3480-3496.https://doi.org/10.1039/C9TB00557A
Ji, C., Lu, J., Shan, B., Li, F., Zhao, X., Yu, J., Xu, S., Man, B., Zhang, C., Li, Z., 2022. The Journal of Physical Chemistry Letters 13(38), 8864-8871.https://doi.org/10.1021/acs.jpclett.2c02392
Jiang, X., Kuklin, A.V., Baev, A., Ge, Y., Ågren, H., Zhang, H., Prasad, P.N., 2020. Physics Reports 848, 1-58.https://doi.org/https://doi.org/10.1016/j.physrep.2019.12.006
Langer, J., Jimenez de Aberasturi, D., Aizpurua, J., Alvarez-Puebla, R.A., Auguié, B., Baumberg, J.J., Bazan, G.C., Bell, S.E.J., Boisen, A., Brolo, A.G., Choo, J., Cialla-May, D., Deckert, V., Fabris, L., Faulds, K., García de Abajo, F.J., Goodacre, R., Graham, D., Haes, A.J., Haynes, C.L., Huck, C., Itoh, T., Käll, M., Kneipp, J., Kotov, N.A., Kuang, H., Le Ru, E.C., Lee, H.K., Li, J.-F., Ling, X.Y., Maier, S.A., Mayerhöfer, T., Moskovits, M., Murakoshi, K., Nam, J.-M., Nie, S., Ozaki, Y., Pastoriza-Santos, I., Perez-Juste, J., Popp, J., Pucci, A., Reich, S., Ren, B., Schatz, G.C., Shegai, T., Schlücker, S., Tay, L.-L., Thomas, K.G., Tian, Z.-Q., Van Duyne, R.P., Vo-Dinh, T., Wang, Y., Willets, K.A., Xu, C., Xu, H., Xu, Y., Yamamoto, Y.S., Zhao, B., Liz-Marzán, L.M., 2020. ACS Nano 14(1), 28-117.https://doi.org/10.1021/acsnano.9b04224
Lee, H.K., Lee, Y.H., Koh, C.S.L., Phan-Quang, G.C., Han, X., Lay, C.L., Sim, H.Y.F., Kao, Y.-C., An, Q., Ling, X.Y., 2019. Chemical Society Reviews 48(3), 731-756.https://doi.org/10.1039/C7CS00786H
Lee, H.K., Lee, Y.H., Zhang, Q., Phang, I.Y., Tan, J.M.R., Cui, Y., Ling, X.Y., 2013. ACS Applied Materials & Interfaces 5(21), 11409-11418.https://doi.org/10.1021/am403655g
Leong, Y.X., Lee, Y.H., Koh, C.S.L., Phan-Quang, G.C., Han, X., Phang, I.Y., Ling, X.Y., 2021. Nano Letters 21(6), 2642-2649.https://doi.org/10.1021/acs.nanolett.1c00416
Li, J.F., Huang, Y.F., Ding, Y., Yang, Z.L., Li, S.B., Zhou, X.S., Fan, F.R., Zhang, W., Zhou, Z.Y., Wu, D.Y., Ren, B., Wang, Z.L., Tian, Z.Q., 2010. Nature 464(7287), 392-395.https://doi.org/10.1038/nature08907
Limbu, T.B., Chitara, B., Garcia Cervantes, M.Y., Zhou, Y., Huang, S., Tang, Y., Yan, F., 2020. The Journal of Physical Chemistry C 124(32), 17772-17782.https://doi.org/10.1021/acs.jpcc.0c05143
Liu, L., Shangguan, C., Guo, J., Ma, K., Jiao, S., Yao, Y., Wang, J., 2020. Advanced Optical Materials 8(23), 2001214.https://doi.org/https://doi.org/10.1002/adom.202001214
Liu, R., Jiang, L., Yu, Z., Jing, X., Liang, X., Wang, D., Yang, B., Lu, C., Zhou, W., Jin, S., 2021. Sensors and Actuators B: Chemical 333, 129581.https://doi.org/https://doi.org/10.1016/j.snb.2021.129581
Liu, X., Dang, A., Li, T., Sun, Y., Lee, T.-C., Deng, W., Wu, S., Zada, A., Zhao, T., Li, H., 2023. ACS Sensors.https://doi.org/10.1021/acssensors.2c02808
Lombardi, J.R., Birke, R.L., 2009. Accounts of Chemical Research 42(6), 734-742.https://doi.org/10.1021/ar800249y
Nie, S., Emory, S.R., 1997. Science 275(5303), 1102-1106.https://doi.org/10.1126/science.275.5303.1102
Niu, W., Zheng, S., Wang, D., Liu, X., Li, H., Han, S., Chen, J., Tang, Z., Xu, G., 2009. Journal of the American Chemical Society 131(2), 697-703.https://doi.org/10.1021/ja804115r
Peng, Y., Lin, C., Long, L., Masaki, T., Tang, M., Yang, L., Liu, J., Huang, Z., Li, Z., Luo, X., Lombardi,

J.R., Yang, Y., 2021. Nano-Micro Letters 13(1), 52.https://doi.org/10.1007/s40820-020-00565-4
Sahin, F., Celik, N., Ceylan, A., Pekdemir, S., Ruzi, M., Onses, M.S., 2022. Chemical Engineering Journal 431, 133445.https://doi.org/https://doi.org/10.1016/j.cej.2021.133445
Sarigul, N., Korkmaz, F., Kurultak, I., 2019. Sci Rep 9(1), 20159.https://doi.org/10.1038/s41598-019-56693-4
Sarycheva, A., Makaryan, T., Maleski, K., Satheeshkumar, E., Melikyan, A., Minassian, H., Yoshimura, M., Gogotsi, Y., 2017. The Journal of Physical Chemistry C 121(36), 19983-19988.https://doi.org/10.1021/acs.jpcc.7b08180
Seo, C., Jang, D., Chae, J., Shin, S., 2017. Scientific Reports 7(1), 500.https://doi.org/10.1038/s41598-017-00497-x
Soundiraraju, B., George, B.K., 2017. ACS Nano 11(9), 8892-8900.https://doi.org/10.1021/acsnano.7b03129
Wang, X., Mathis, T.S., Sun, Y., Tsai, W.-Y., Shpigel, N., Shao, H., Zhang, D., Hantanasirisakul, K., Malchik, F., Balke, N., Jiang, D.-e., Simon, P., Gogotsi, Y., 2021a. ACS Nano 15(9), 15274-15284.https://doi.org/10.1021/acsnano.1c06027
Wang, X., Wang, Z., Qiu, J., 2021b. angewandte Chemie International Edition 60(51), 26587-26591.https://doi.org/https://doi.org/10.1002/anie.202113981
Westley, C., Xu, Y., Thilaganathan, B., Carnell, A.J., Turner, N.J., Goodacre, R., 2017. Analytical Chemistry 89(4), 2472-2477.https://doi.org/10.1021/acs.analchem.6b04588
Xie, H., Li, P., Shao, J., Huang, H., Chen, Y., Jiang, Z., Chu, P.K., Yu, X.-F., 2019. ACS Sensors 4(9), 2303-2310.https://doi.org/10.1021/acssensors.9b00778
Yang, K., Zhu, K., Wang, Y., Qian, Z., Zhang, Y., Yang, Z., Wang, Z., Wu, L., Zong, S., Cui, Y., 2021. ACS Nano 15(8), 12996-13006.https://doi.org/10.1021/acsnano.1c01890
Yang, S., Dai, X., Stogin, B.B., Wong, T.-S., 2016. Proceedings of the National Academy of Sciences 113(2), 268-273.https://doi.org/doi:10.1073/pnas.1518980113
Yao, L., Dai, P., Ouyang, L., Zhu, L., 2021. Microchemical Journal 160, 105728.https://doi.org/https://doi.org/10.1016/j.microc.2020.105728
Ye, Y., Yi, W., Liu, W., Zhou, Y., Bai, H., Li, J., Xi, G., 2020. Science China Materials 63(5), 794-805.https://doi.org/10.1007/s40843-020-1283-8
Yunker, P.J., Still, T., Lohr, M.A., Yodh, A.G., 2011. Nature 476(7360), 308-311.https://doi.org/10.1038/nature10344
Zhang, C., Ji, C., Yu, J., Li, Z., Li, Z., Li, C., Xu, S., Li, W., Man, B., Zhao, X., 2021. Opt. Express 29(23), 38768-38780.https://doi.org/10.1364/OE.441176
Zhang, C., Li, Z., Qiu, S., Lu, W., Shao, M., Ji, C., Wang, G., Zhao, X., Yu, J., Li, Z., 2022. Nanophotonics 11(1), 33-44.https://doi.org/doi:10.1515/nanoph-2021-0476
Zhao, Y.-Y., Ren, X.-L., Zheng, M.-L., Jin, F., Liu, J., Dong, X.-Z., Zhao, Z.-S., Duan, X.-M., 2021. Opto-Electronic Advances 4(12), 200101-200109.https://doi.org/10.29026/oea.2021.200101